

# Influence of Structural Elements and Stress on Mining-Induced Fault Slip

Chen Lin · Deyong Guo · Yueqiang Liang

Received: 21 March 2017 / Accepted: 14 August 2017 / Published online: 20 August 2017  
© Springer International Publishing AG 2017

**Abstract** This study examines the relationships between the structural elements, stress state and fault slip at the No. 8 mine in the Pingdingshan area, northern China. Based on a geological environment investigation of the field and the structural setting of the mine, two tectonic zones are identified as hosts to numerous fault slip events. The spatial distribution of events is closely linked to horst structures, but different types of horst structures may represent different mechanisms of fault dynamic fault behavior. Almost all of the fault slip events are concentrated in the region with steep orebody dip gradients, and the radius of curvature shows an impressive correlation with the cumulative occurrence of fault slip. Geophysical information of fault surfaces is used for stress reconstruction to estimate the orientation of the principal stresses. The results obtained from this analysis show that the principal stress oriented NNE–NE exerts the primary control in the western region of the field, yet the principal stress oriented NWW–NW strongly influences the middle region of the field. The analysis conducted here may be easily applied to other underground developments in structural zones and may show a positive effect on assessment of fault slip hazard.

**Keywords** Geological environment · Structural element · Geophysical information · Stress · Fault slip

## 1 Introduction

Within the past several decades, there has been an increasing demand for energy resources such as mineral resources. Deep mining activity is common, and it is inevitable that due to the extraction of mineral deposits from great depths, fault and fracture zones will need to be transected (Hatherly 2013). However, when geologic structures exist in underground mining environments, problems related to the rock mass and fault of active structural zones occur frequently. These problems seriously influence mineral production and safety of underground personnel (McGarr et al. 1989; Kalaneh and Agh-Atabai 2016; Wang et al. 2016). Based on a previous analysis of the differences between disturbed and undisturbed districts, the largest magnitude mine tremors have been determined to have occurred in a faulted area of South Africa. Feit et al. (2002) have estimated the rock burst hazard by determining the rock mass energy in the Kuznetsk Basin.

Coulson (1996) considered the relationship between highly stressed ground and mine-induced seismicity using PCA (principal component analysis). In an attempt to investigate shear stress on the San Andreas fault at depth. Zoback et al. (1980) measured

---

C. Lin (✉) · D. Guo · Y. Liang  
School of Resources and Safety Engineering, China  
University of Mining and Technology, No. 11 Xueyuan  
road, 100083 Beijing, China  
e-mail: crazylinchen@163.com

the variation in shear stress with distance from the fault in relatively shallow wells. Tectonism and stress states in active structural areas are strongly related to the regional and local stresses (Zeng and Liu 2009; Yadav et al. 2016; Terakawa et al. 2013; Bonini 2012), providing constraints for the orientation of faults and fractures and location of fault slip burst. Fault slip burst may be caused by a significant stress redistribution and rotation due to mining-induced stress and in situ stress around mine openings. Thus, when interpreting faulted zone stability and forecasting fault slip burst occurrence, these two fundamental aspects should be taken into consideration.

Cai et al. (2004) proposed that the crack initiation and crack damage stress threshold is defined by a material constant and uniaxial compressive strength of the rock mass by examining data from both intact and jointed rock masses. The mechanical properties of faulted zones are greatly affected by many factors that are not easy to clearly define (Oettlea et al. 2015). Despite efforts made to comprehend the mechanical behavior of faults and rock joints, the scale effect on the mechanical properties of structural zones is still obscured (Barton 1982). Fault damage zones result from the propagation of fault tips through a rock or from damage associated with the increase in slip on a fault, and the damage zone structures are distributed along the fault trajectories in map view (Kim et al. 2004). Fault slip burst is a special type of underground disaster that is generated by sliding of a preexisting fault in mining-induced active geological zones. To understand the mechanism of fault slip burst, the characteristics and prediction of fault slip have been studied by many researchers using physical and mechanical properties of faults, numerical simulations, and physical experiments with similar material properties (Sainoki and Mitri 2014; Ma et al. 2002; Michael et al. 2009).

As mentioned above, the role of geological structure and stress on fault slip burst has not yet been fully understood. It is evident that combining data derived from these two areas is essential to clarify the mechanism of fault slip burst and predict future induced fault slip events.

This study analyzes the fault slip events and time-dependent rock degradation in order to determine the correlation between fault slip burst and geological structure in the Pingdingshan No. 8 mine. Structural elements (type of geological structure, terrain

curvature and dip of ore deposits) are taken into consideration and might exert an influence on the fault slip. Geophysical information on fault surfaces is used for stress reconstruction to determine estimates of the orientation of the principal stresses. The results of the stress reconstruction from geophysical information are used to assess its control on two clusters of fault slip events.

## 2 Geological Data

### 2.1 Regional Framework

The Pingdingshan No. 8 mine is situated in the eastern Pingdingshan coalfield, which is a large coal producer in northern China (Fig. 1). The Pingdingshan coalfield is located on the northern margin of the Qinling orogenic belt, which is defined as a thrust nappe structure system in the southern North China Block (Zhang 2009). The tectonic history of this coalfield is closely related to the Likou syncline, which intersects the northern tip of the No. 8 mine (Li 2001). The Likou syncline is subordinate to the Qinling orogenic belt and extends approximately 50 km from the Jiaxian fault, northwest of the Pingdingshan coalfield and east of the Luogang fault (Fig. 1). The Likou syncline strikes west to northwest and dips between 8° and 12°.

The coal-bearing sediments in the formations along the Likou syncline are primarily from Permian period, followed by repeated strike-slip movement during the Yanshanian Orogeny and sinistral-oblique faulting in the Himalayan period. The hanging wall rocks mainly consist of medium, fine and silty sandstone. The footwall rocks surrounding the coal seam are composed of interbedded sand and shale (Fig. 2). The coalfield is characterized by folds, normal faults and strike-slip faults. The majority of faults strike NW (in the eastern and western margin of the coalfield), NE (in the middle of the coalfield), or approximately EW (dispersed and rarer), although abundant N–S structures were also detected in a morphometric survey (Geological survey of Henan province 1990).

In the middle and western areas of the region, geophysical data have highlighted an array of tectonic structures, including anticlines, synclines and unconformities. The ongoing compressional tectonic activity and a large number of hidden faults were identified by previous excavation studies, which support the idea

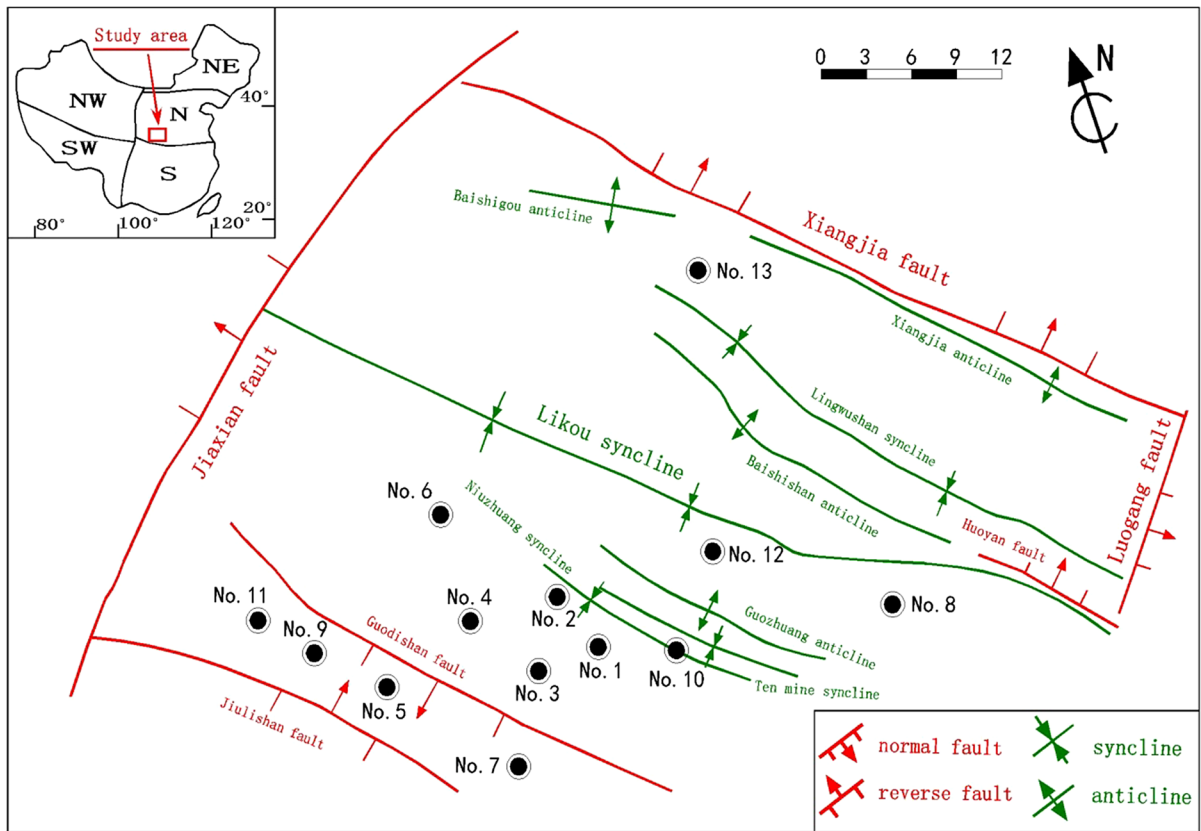


**Fig. 1** Schematic structural map of the Pingdingshan coalfield

that the sedimentary rocks are fractured or weak (Qu 2010). If these characteristics are observed to intensity within a narrow zone, it is regarded as a potential slip zone. Historical fault slip distribution and dominant SEM (scanning electron microscope) photomicrographs suggest that severe damage to a rock mass plays an important role in the fault slip generation (Fig. 3).

### 2.2 Structural Setting of the Pingdingshan No. 8 Mine













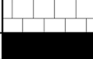




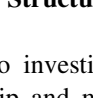
The Pingdingshan No. 8 mine is located along the axis of the southeastern Likou syncline and is in a tectonic zone characterized by a strong variation in schistosity and lineation direction. Deep in the No. 8 mine, ore bodies occur along strike in the northwest-trending folds in the hinge, where the limbs change from gently dipping to steeply dipping. Composite foliation and extensional lineation are also widespread in this region, and the fabric of the rocks show mainly

penetrative extensional deformation (Frodsham and Gayer 1999).

Three families of tectonic zones are mapped: northwest-striking tectonic zone (including the Likou syncline, Guozhuang anticline, Shiyikuang fault, Niuzhuang fault, Niuzhuang syncline, Renzhuang fault, Zhangwan fault, and Baishigou fault), north-south-striking Jiaozan syncline, and north-east-striking tectonic zone (including the Xindian fault, and Qiannie anticline). The Likou syncline and Guozhuang anticline in the northwest-striking tectonic zone are the most continuous structures (Fig. 5).

Mylonitic textures are widespread in the areas with compressive and shear deformation and are in ductile shear structures or compressive structures such as small-scale vergent folds and thrust ramps. Buried faults identified around the Guozhuang anticline and along its fold trace can be generally subdivided into a fold-orthogonal set and a fold-parallel set, but the fault throw is commonly small, between 1 and 5 m. The distribution of the faults shows distinct spatial trends. The largest

**Fig. 2** Geology columnar section of Pindingshan coalfield

Geologic age	Average depth (m)	Average thickness (m)	Graphic	Explanation
Quaternary	35.2	35.2		Clay, mud, sand with gravel and calcrete
Tertiary	42.7	7.5		Argillaceous limestone dominant
Permian	97.3	54.6		Red continental clastic rock
	130.5	33.2		sandstone
	133.1	2.6		Ding coal seam
	136.2	3.1		medium sandstone
	188.8	52.6		fine sandstone
	236.6	47.8		silty sandstone
	242.8	5.8		Wu coal seam
	305.4	62.6		silty sandstone
	399.2	93.8		mudstone
	402.0	2.8		Ji coal seam
	417.2	15.2		Transitional facies
Carboniferous	456.3	39.1		Marine-continental alternative facies
	457.9	1.6		Geng coal seam
	466.5	8.6		Aluminous mudstone dominant
	474.3	7.8		Bedded carbonate rock
Cambrian				Bedded limestone of neritic facies with oolitic limestone

number of faults are found directly to the west of this field. A moderate number of faults are observed in the middle of this field. The lowest number of faults are observed to the east of this field. The orientation of the buried faults obtained from underground excavation have been plotted on a rose diagram, shown in Fig. 4. The faults in the western area are dominantly orientated NNW to NW. On the contrary, the faults in the middle and eastern areas show an indefinite trend, which does not suggest consistent fault orientation. This lack of a common fault orientation suggests that fault slip events do not occur on similarly oriented faults and have no relationship with the geological structure within the middle and eastern part of the anticline.

### 3 Structural Controls on the Fault Slip

To investigate the possible relations between fault slip and mapped tectonic zones in the No. 8 mine deep, 39 fault slip events that occurred between 424 and 840 m depth are used to analyze the factors that may have had an influence on the behavior of fault slip, such as the types of geological structures, terrain curvature and dip of the ore deposits. The events caused by mining activity are observed to cluster spatially around the mining openings and fade away rapidly; these are not included in this research. In the following sections, detailed descriptions of the three factors are given.

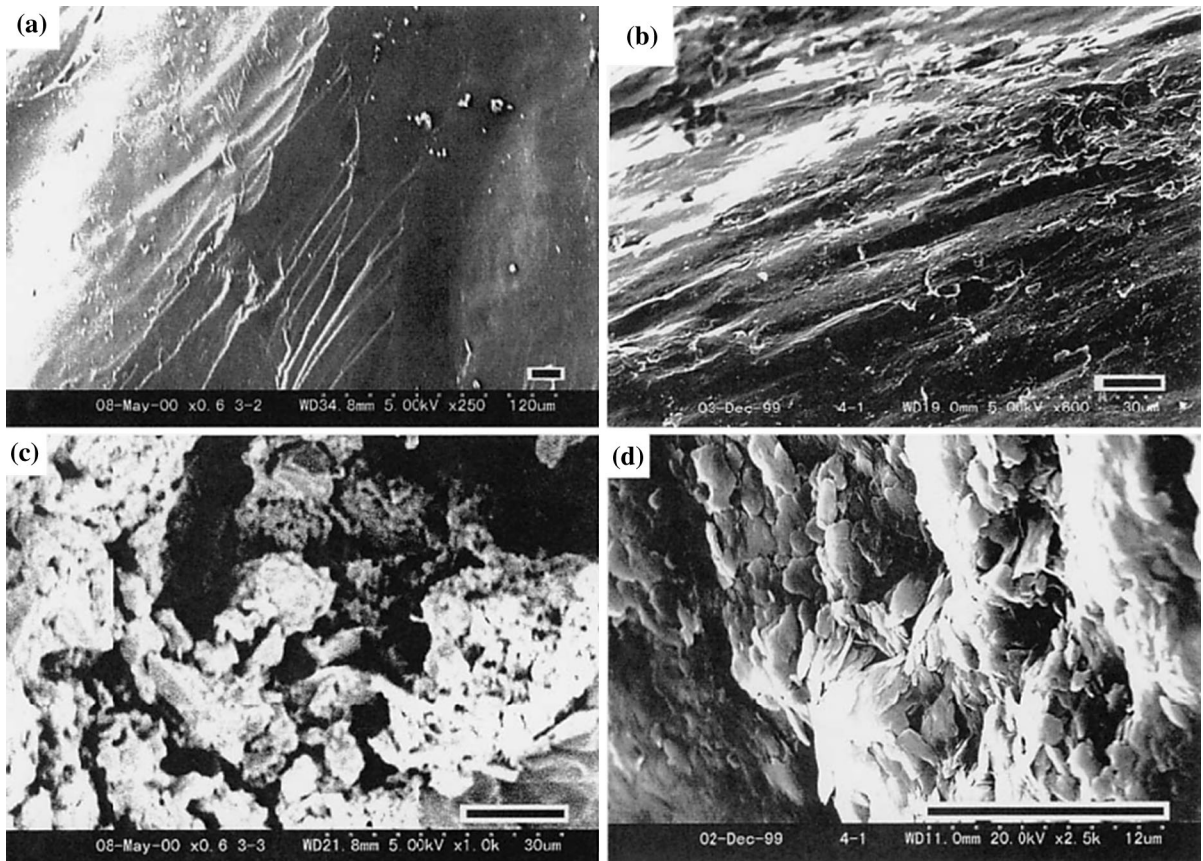


**Fig. 3** SEM photomicrographs of coal. All samples were obtained from the Pingdingshan coalfield. **a** Non-tectonic fracture surface with little damage. **b** Slickenside of a highly

polished coal. **c** Brittle failure in coal with honeycomb-like pores. **d** Extensively sheared coal. The scale bar is 12 mm in length

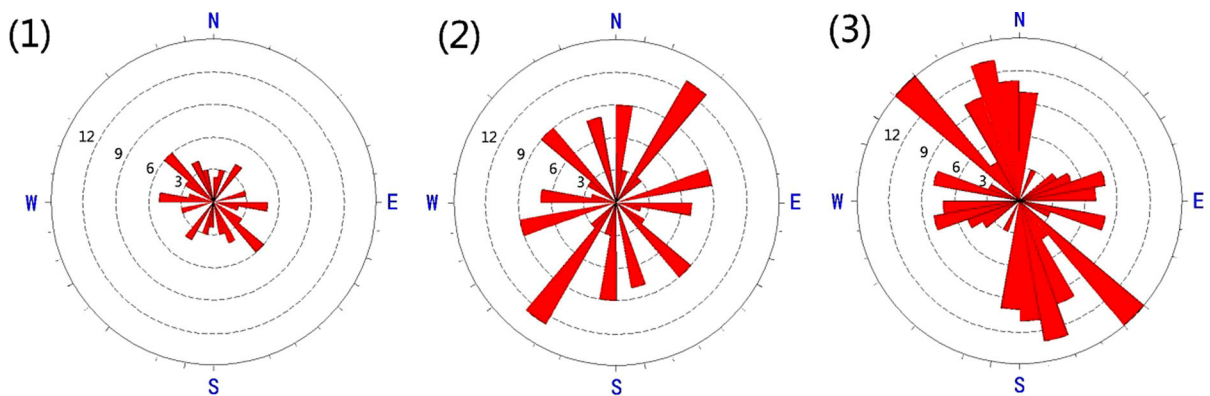


**Fig. 4** Statistical analysis of buried fault in No. 8 mine. **1** Rose diagram of east of the field. **2** Rose diagram of middle of the field. **3** Rose diagram of west of the field



### 3.1 Relations Between Fault Slip and Types of Geological Structures

Fault slip may be controlled by a variety of tectonic elements and structural mechanisms acting at various length scales. Furthermore, fault slip events are likely to be distributed over a large portion of fold-and-fault belts and other discrete regional-scale structures (correlated to the Likou syncline of the Qinling orogenic system and inferred to share a common tectonic heredity). The types of geological structure within the mine include normal faults, thrust faults, folds, shear structures, and cleavage duplexes. These tectonic elements are closely linked to the regional stress field, and are also inferred to exert some control on the paroxysmal events the fault may experience.

The axis of the Likou syncline trends generally NW–SE, and is the predominant structure regarding mining operations. The majority of faults are either reverse or normal and strike NW–SE. Deformation of the NW–SE trending compressive structures is common and drives fault slip, which may exhibit remarkable differences in spatial distribution. Within these events, two spatial clusters of events that are close to the structural zones are identified clusters 1 and 2 (Fig. 5). Cluster 1 is located in the northern limb of the Guozhuang anticline, in which 24 events have been triggered by mine development. Conversely, the 15 events of cluster 2 were induced by ore excavation in a splay area between the Xindian fault and Zhangwan fault. Based on the displacement from stratigraphic boundaries studies, it is suggested that cluster 1 localized along the northern flank of a thrust zone,

and cluster 2 localized in a narrow belt formed by the Xindian and Zhangwan faults.

The geometry of the fault configuration exerts a clear influence on the formation of ore deposits and ultimately on fault slip. A thrust zone is created from the Shiyikuang and Niuzhuang faults, which includes only thrust faults (Fig. 6). These main faults dip in opposite directions, and the dipping of the Shiyikuang fault is steeper than that of the Niuzhuang fault. The morphologic characteristic of the thrust zone shows that the rock strata can be regarded as a horst structure system. In Fig. 7, the narrow belt is made from the interaction of two normal faults (Xindian and Zhangwan). The Xindian fault dips steeply to the north between  $65^\circ$  and  $75^\circ$ , and the Zhangwan fault exhibits a comparatively gently dip at  $38^\circ$ . In terms of the structural form, this narrow belt is consistent with the thrust zone mentioned above and can be defined as a horst structure. Although cluster 1 and 2 represent the same structural classification, the geometry of the fault configurations suggests extremely different structural mechanisms between the two clusters. The former configuration is a reverse trapezoid, and the latter is a regular trapezoid.

### 3.2 Terrain Curvature Analysis of the Fault Slip

Terrain curvature is a quantitative representation of a terrain's surface morphology and is widely used to evaluate the complexity of topographic features. A well-established link between topographic features and structural deformation is commonly applied to understand geohazards (Roberts 2001; Marfurt 2006).

**Fig. 5** Structural outline of No. 8 mine

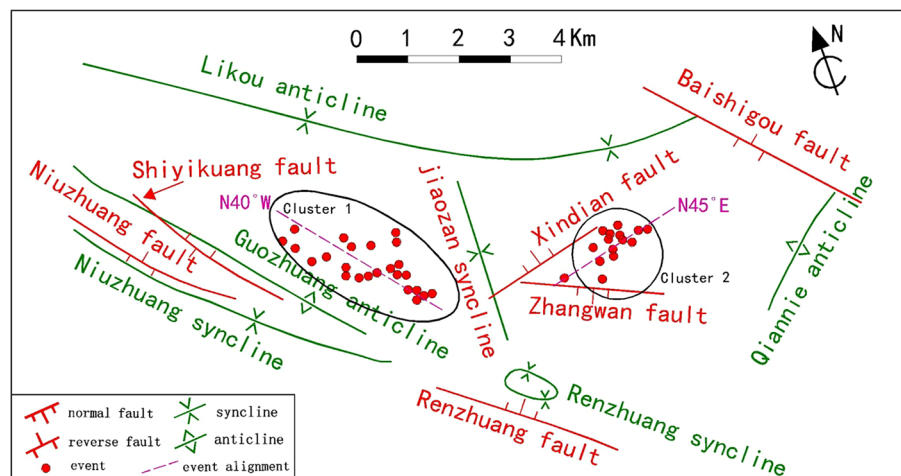


**Fig. 6** Structural cross-section shows the geological geometry of Cluster 1

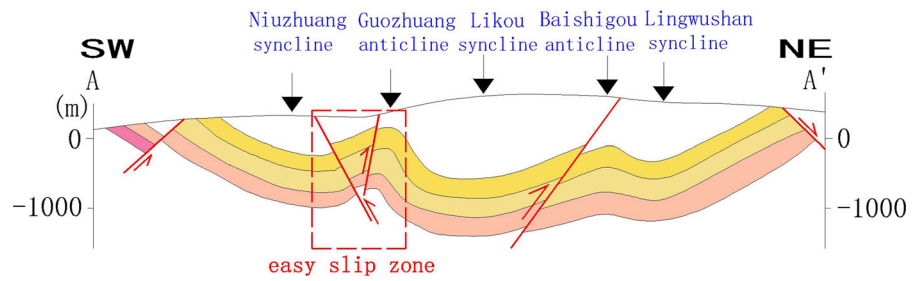
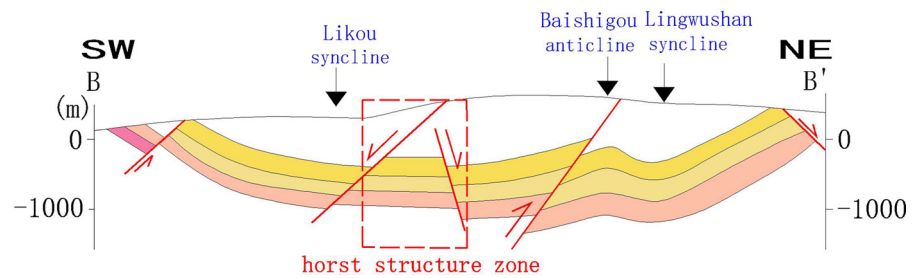


**Fig. 7** Structural cross-section shows the geological geometry of Cluster 2



Therefore, in the present study, this parameter (terrain curvature) can be adopted as an indicator to investigate the interaction between fault slip and tectonic structures. Successful calculation of terrain curvature calls for the collection of relevant spatial data, and in this study, the data are obtained from a gas geology database compiled at the Geological Survey of Pingdingshan. The terrain curvature,  $k$  is given by

$$k = \frac{\frac{d^2y}{dx^2}}{\left[1 + \left(\frac{dy}{dx}\right)^2\right]^{\frac{3}{2}}} \tag{1}$$

The radius of curvature,  $r$  is given by

$$r = \frac{\left[1 + \left(\frac{dy}{dx}\right)^2\right]^{\frac{3}{2}}}{\frac{d^2y}{dx^2}} = \frac{1}{k} \tag{2}$$

where  $\frac{d^2y}{dx^2}$  is the second derivative and  $\frac{dy}{dx}$  represents the first derivative of a curve in the terrain.

One way to visualize curvature is through a particular stereogram, as displayed in Fig. 8. In this figure, the geomorphic features shown include an anticline, syncline and a flat horizon. The curvature is defined as zero, where the horizon is flat or a dipping plane. The sign conventions used in this paper are positive curvature for the crests of anticlines and negative curvature for the syncline hinge zones.

The calculated results of the terrain curvatures of cluster 1 and cluster 2 are given in Fig. 9. The

horizontal and vertical axes in the figures represent the fault slip number and curvature, respectively. As can be seen, there is a clear difference in the curvature distribution between cluster 1 and cluster 2. First, for cluster 1, the curvature of events 12, 22 and 23, decreases from positive to negative. In contrast, for cluster 2, all the curvature is negative, although event 7 and 12 fluctuate significantly. Figure 10a depicts the relation between the amount of events and radius of curvature. The effect of the radius of curvature on the occurrence of fault slip seems to be ambiguous. However, it is evident from the results of intervals 1, 2, and 3 that the amount of events increases with an increasing radius of curvature. For a better understanding of the relationships, the proportional distribution is plotted in Fig. 10b. As seen in the figure, both of interval 2 and interval 3 are strongly affected by the occurrence of fault slip. Thus, in terms of the prevention of fault slip, it can be concluded that the radius of curvature ranging from  $1.0 \times 10^4$  to  $3.0 \times 10^4$  is undesirable.

### 3.3 Dip Analysis of the Fault Slip

The dip of the ore deposits is a two-dimensional property and can describe the state and azimuth of rock strata at a particular point. A steeply dipping deposit frequently causes dynamic behavior of in fault zones (Bewick et al. 2009). In this study area, a marked

**Fig. 8** Sign convention for curvature attributes

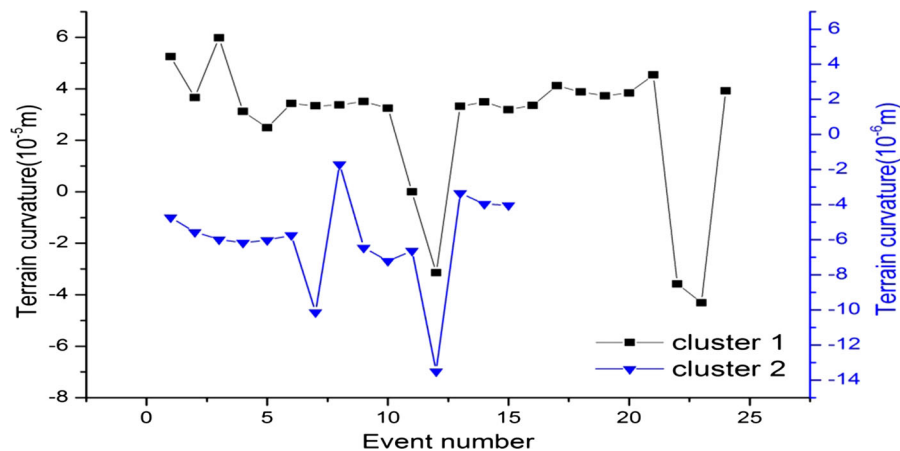
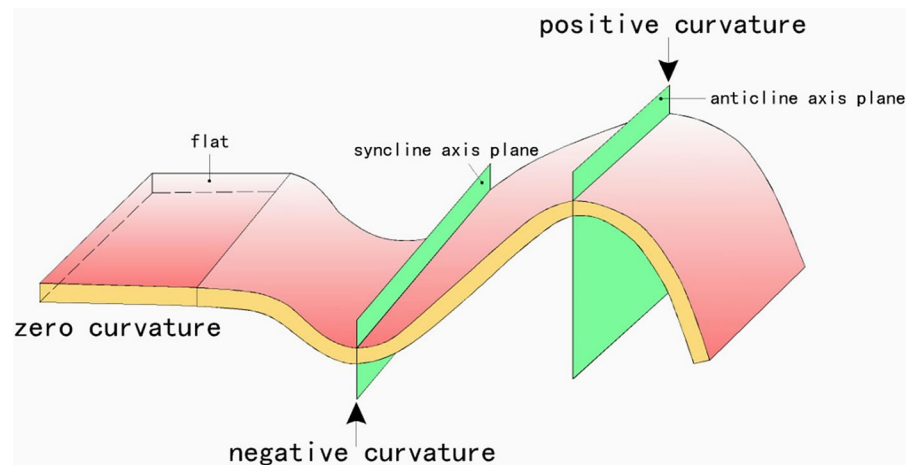


**Fig. 9** Scatter diagram shows the calculated terrain curvatures of cluster 1 and cluster 2

variation in the dip of the ore deposits occurs between different locations, even within the same underground mine. Figure 11 shows the distribution of the dip of the ore deposits and includes all the fault slip events recorded to date. Two main areas are observed with notably steep ore deposit dips, compared to the other areas. One area is in the north flank of the Guozhuang anticline, with dips of 14–24, and the other is in the interaction area of the Xindian and Zhangwan faults, with dips of 12–18. We observe that many fault slip events concentrate at the rim of the rock stratum, where dip gradients of the orebody are steep, rather than within the interior of the inclined rock stratum. Cluster 1 strikes in a N40°–45°W direction, which trends subparallel to the axis of the Guozhuang

anticline. However, cluster 2 strikes N45°–50°E alignments, which trends suborthogonal to the axis of the Jiaoan syncline (Fig. 5).

## 4 Stress State and its Relations with the Fault Slip

### 4.1 Stress State Reconstruction Procedure

Using different types of geophysical information of fault surfaces determined from slickensides, the orientation of stress axes can be reconstructed (Angelier 1979; Angelier et al. 1982; Angelier 1984; Shi et al. 2015). This method utilizes observed slickenside directions and senses of motion of fault planes and



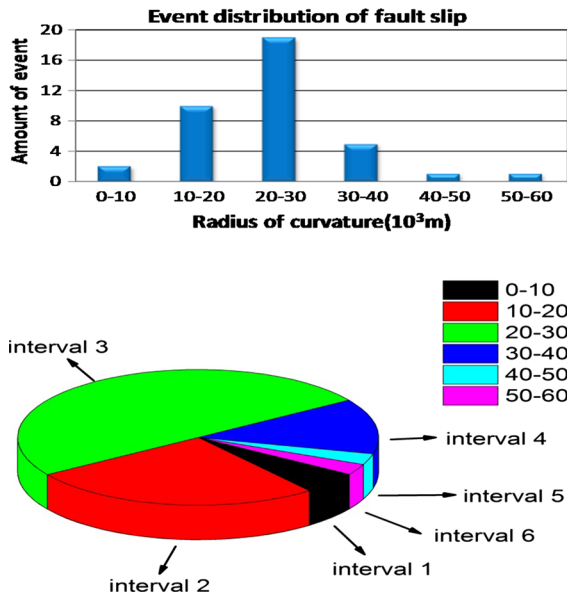


**Fig. 10** a Histogram shows the relation between the distribution of fault slip and radius of curvature. b Diagram shows the percentage of different interval

compares calculated solutions to find a best fit between the shear stress and sense of motion, with minimal error (Etchecopar et al. 1981).

The stress tensor of any point in space can be described with horizontal coordinate system (OXYZ):

$$T = \begin{bmatrix} \sigma_1 & 0 & 0 \\ 0 & \sigma_2 & 0 \\ 0 & 0 & \sigma_3 \end{bmatrix}$$

where  $T$ ,  $\sigma_1$ ,  $\sigma_2$  and  $\sigma_3$  are the stress tensor, maximum principal stress, intermediate principal stress and minimum principal stress, respectively.

According to the basic theory of elastic mechanics, a stress tensor can be decomposed into a spherical stress tensor and deviatoric stress tensor, as follows:

$$T = P + D \tag{3}$$

where  $T$ ,  $P$  and  $D$  are the stress, spherical stress and deviatoric stress tensors, respectively. Since the spherical stress tensor just influences the normal stress on a fault surface, the deviatoric stress tensor dominates tangential stress along the fault.  $f$  represents stress on the fault surface, and  $n$  is the normal vector perpendicular to the fault plane. The stress component of  $f$  in the  $u$  direction is represented by  $f_u$ . Similarly,  $f_s$  represents the stress component of  $f$  in the  $s$  direction.  $\tau$  indicates the estimated shear stress along a fault. The unit vector of shear stress is  $t$  (Fig. 12).

As shown in Fig. 13,  $n$  is the normal vector perpendicular to the fault plane. The dashed lines colored in different shades of blue in Fig. 13 indicate the direction of fault slickensides. As in the expression in Fig. 12,  $\tau$  represents the direction of the predicted shear stress, and  $f$  represents the complex stress on the fault surface.

As shown in Fig. 12, the stress on the fault surface is computed as follows:

$$f = T \cdot n \tag{4}$$

The shear stress is determined to be

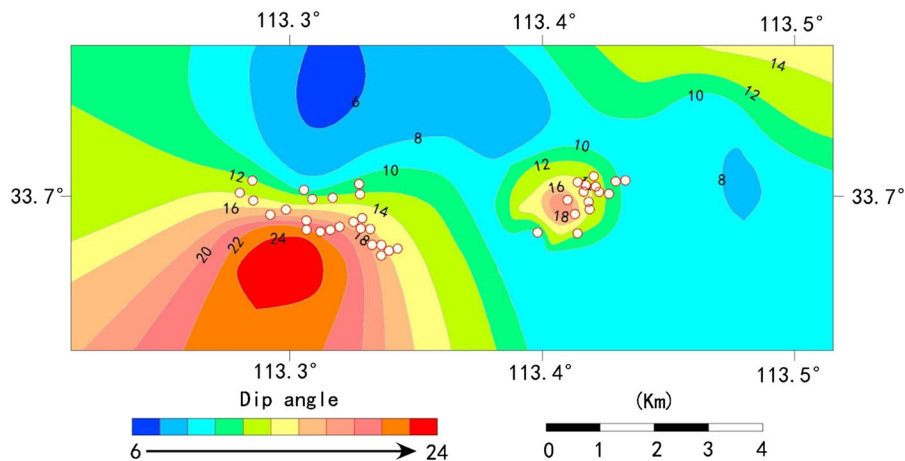


**Fig. 11** The relationship between dip isoline and fault slip event

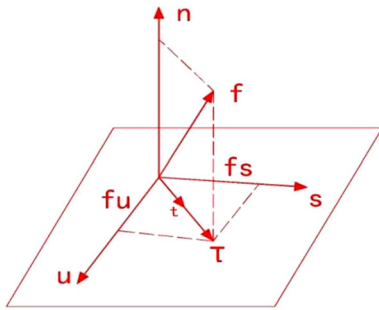


**Fig. 12** Geometric relationships in stress distribution of fault

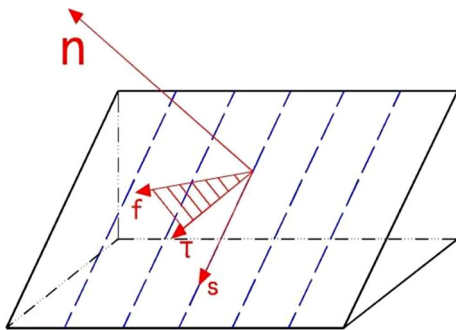


**Fig. 13** Schematic representation of sliding behaviour on fault surface

$$\tau = f - (f \cdot n)n = T \cdot n - (n \cdot T \cdot n)n \quad (5)$$

where  $\tau$ ,  $f$ , and  $n$  are the shear stress, stress on the fault surface and normal vector of the fault plane. Thus, the corresponding unit vector of shear stress can be expressed by

$$t = \frac{\tau}{|\tau|} = \frac{T \cdot n - (n \cdot T \cdot n)n}{|T \cdot n - (n \cdot T \cdot n)n|} \quad (6)$$

The purpose of this method is find a best-fit stress tensor that minimizes the angle between the shear stress and direction of the fault slickensides.

Individual stress reconstruction for the western and middle regions of the field is performed, excluding the eastern region. This decision is mainly based on two aspects: one is that the eastern region has few valid fault slickensides, and the other is that there is no fault slip event occurrence. Although there are some irregular results shown in Fig. 14, in general, it is apparent from the detailed stress data that there are clear indicators of the direction of the principle stresses.

## 4.2 Relations Between the Stress State and Fault Slip

Based on the results of the stress reconstruction from the geophysical information of the fault surfaces, the directions of the minimum and maximum principle stresses are shown in Fig. 14. As seen from the results of the western region of the field, only three results of the maximum principal stress direction are remarkably different than the majority of the results and indicate the orientation NNW. The majority of the results of the maximum principal stress directions indicate a dominant NE to NEE trend, which is roughly perpendicular to the trend of the regional faults and folds (such as the Guozhuang anticline and Likou syncline). These stress orientation results are consistent with the earthquake focal mechanism inversions that strike  $N75^\circ$  and plunge  $14^\circ$  (Table 1). This finding implies that the local stress field is not affected by either the structural elements or the stress deviation induced by stope extraction.

As seen from reconstruction results of the middle region of the field, six results represent a preferential orientation around  $N35^\circ$ , and the rest of the fifteen results are dominantly oriented NW to NNW. The stress orientation can be generally considered NW to NNW, although several stress directions trend NE. This finding demonstrates that the direction of the maximum principal stress in the middle region is almost perpendicular to that in the western part of the field. Thus, it is evident that this change is intimately linked to nearby geological elements and is probably related to a structurally controlled stress redistribution.

Results from the west of the field reconstruction reveal that the maximum principal stress is oriented  $N55^\circ$  with a subhorizontal plunge ( $9^\circ$ ), the intermediate principal stress has an approximately vertical plunge ( $75^\circ$ ) towards  $N151^\circ$ , and the minimum principal stress is oriented  $N301^\circ$  and plunging  $8^\circ$ . These principal stress directions are in good agreement with the stress data measured by the hollow inclusion stress release method (maximum principal stress is oriented  $N061^\circ$  and plunging  $7^\circ$ , intermediate principal stress is oriented  $N155^\circ$  and plunging  $68^\circ$ , and minimum principal stress is plunging  $3^\circ$  towards  $N311^\circ$ ), as exhibited in Fig. 15 and summarized in Table 1.

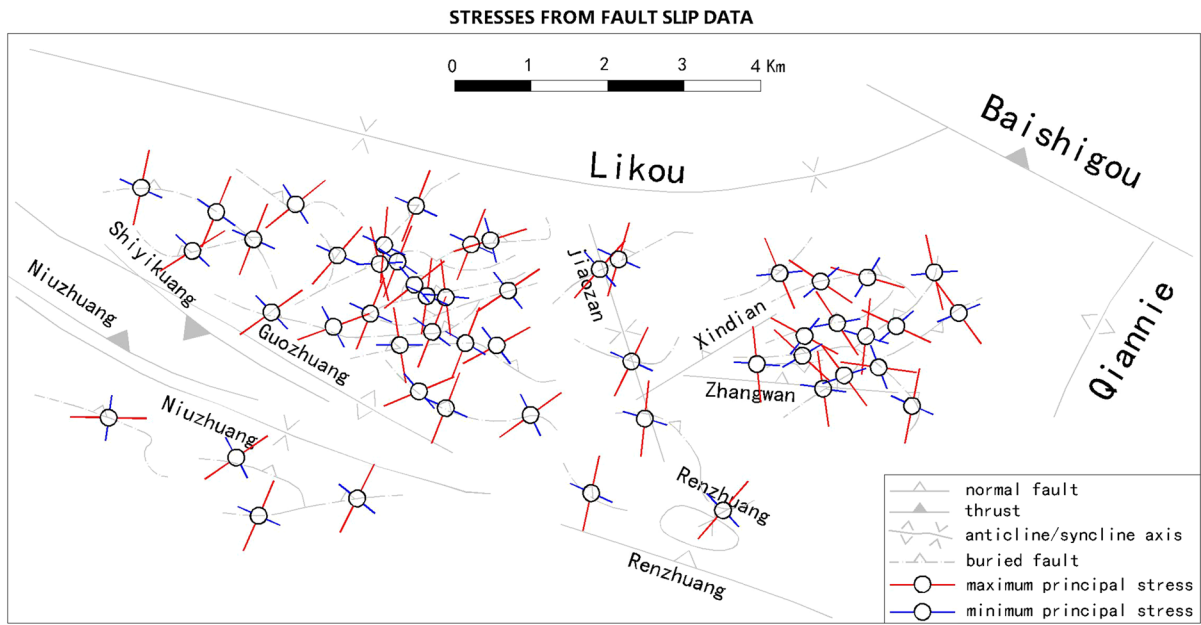


**Fig. 14** Distribution of local minimum and maximum principle stresses reconstructed from fault slip data

**Table 1** Stress results compared to inverted and measured tensors

Result type	Principal stress	Trend	Plunge
Focal mechanism inversion (Xie et al. 2002)	$\sigma_1$	075	14
	$\sigma_2$	180	73
	$\sigma_3$	338	17
Measured stress (Sun 2014)	$\sigma_1$	061	7
	$\sigma_2$	155	68
	$\sigma_3$	311	3
Reconstructed result (west of the field)	$\sigma_1$	055	9
	$\sigma_2$	151	75
	$\sigma_3$	301	8
Reconstructed result (middle of the field)	$\sigma_1$	332	18
	$\sigma_2$	238	12
	$\sigma_3$	095	69

Reconstruction of the middle of the field produces a tremendously different stress information with a maximum principal stress that orients NNW (N332°) with a gentle plunge (18°), an intermediate stress plunges 12° towards N238°, and near-vertical minimum stress that trends EW (N095°) plunging 69° (Fig. 15). The significant rotation of the stress information of middle of the field compared to the inverted and measured results suggests that stress state is unlikely related to regional stress field.

### 5 Discussion

The spatial distribution of fault slip events in the No. 8 mine are closely linked to horst structure zones, but different types of horst structures may represent different mechanisms acting on the dynamic fault behavior. The horst structure in cluster 1 is composed of two thrust faults that dip in opposite directions. According to the structural cross-section, this type of horst is a reverse trapezoid and is plotted in Fig. 16a.

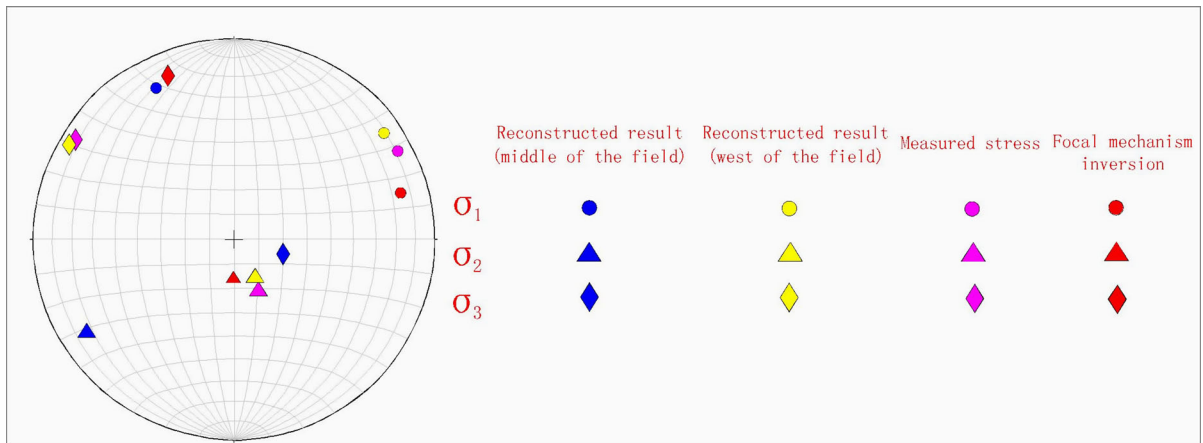


**Fig. 15** Lower hemisphere stereonet shows comparison between reconstructed results and measured stress information and stress tensor inversion of focal mechanism data

The gravitational potential energy of the overlying rockmass tends to be released by the extraction of the slope; however, the stress component perpendicular to the fault surface from the overburden stress in a compressive state. As a result, the force of friction on the fault surface will be comparatively high and strengthen the failure envelope under this circumstance. Nevertheless, the horst structure in cluster 2 is formed by two normal faults that are steeply dipping. As seen in Fig. 16b, this type of horst is a regular trapezoid. The gravitational potential energy of the overburden rock starts to change during the extraction of slope, and the stress component perpendicular to the fault surface from the overburden stress is in a state of extension. In this case, the effect of friction on a fault surface will be estimated to be extremely low, that is to say, it is likely to fail; in a Mohr circle diagram, this failure is illustrated as the Mohr circle of the fault touching the failure envelope. This result is basically

consistent with the analytical solution for horst structure based on the elastic shear beam model (Xiaoqing et al. 2015).

The terrain curvature of the events shows almost a non-linear relationship with the occurrence of fault slip, and this result implies that identifying the connection between the possibility of fault slip and terrain curvature is quite difficult. However, the radius of curvature ranging from  $1.0 \times 10^4$  to  $3.0 \times 10^4$  has a good correlation with the cumulative occurrence of fault slip, although some specific locations do not coincide with this dynamic behavior. This finding indicates that radius of curvature research could be applied to the prediction of fault slip risk.

The two main areas with clearly steep ore deposit dips, located in this zone of frequent fault activity, closely correspond to the two spatial clusters of events, identified as clusters 1 and 2, that are close to the structural zones. This finding indicates that the dip of

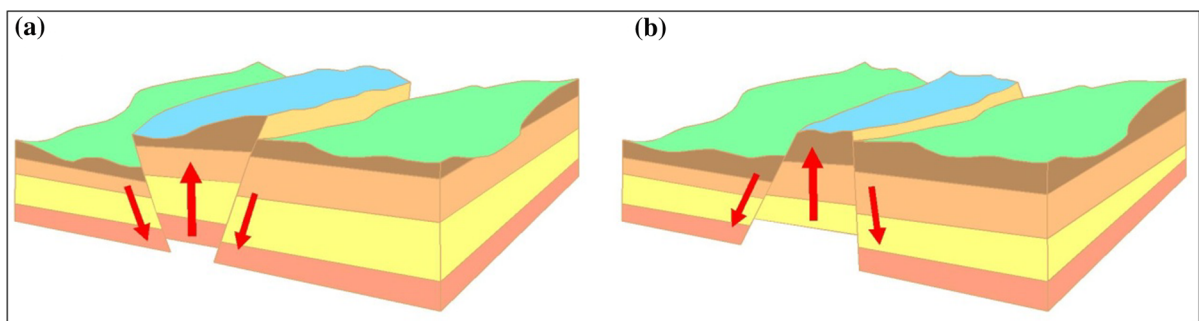


**Fig. 16** Sketch map showing the different type of horst structure. **a** horst structure formed by two thrust faults. **b** horst structure formed by two normal faults

ore deposits may exert a significant influence on fault slip. Moreover, a large proportion of events occurred at areas with steep dip gradients, including the edges of a transition zone, where the dip of ore deposits changes rapidly. A similar phenomenon has also been obtained from a physical rock model of non-persistent joints (Prudencio and Jan 2007), in which the models with smaller fault dips were stronger, and we assume the same failure mode. Buried faults can increase the deformation intensity of rock (Guo and Zeng 2015). The fault slip events at the edge of the transition zone would be triggered by a decrease in fault strength in the strong deformation zone.

Alignments of active fault slip events have been analyzed to identify the structural setting in which a fault slip occurred (Fehler 1990). Note, however, that the quality of event alignments do not always correspond to the measured and inverted results. The presence of such NW- and NE-trending fault slip event alignments cannot be easily understood. One possible explanation is that the NE alignment preferentially developed a NE-trending bedding structure along the preexisting joints. The NW-trending set could be correlated to fold-forming stresses since this set is perpendicular to the compressive stress axis. The bedding faults deform the mineral deposits and can be referred to as sliding structures. The NE alignment is formed by two oppositely dipping normal faults creating a sort of horst structure that closely follows the trend of the syncline axis. The bedding faults display an apparent fault throw of up to 5 m, and are characterized by comparatively fresh slickensides. These bedding faults are similar to the sliding structures and seem to induce fault slip and collapse of the horst structure. Therefore, the bedding faults are most likely structurally controlling the NE alignment of the fault slip events.

The stress reconstruction result of the stress state in the western region of the field, where cluster 1 is located, is consistent with the principal stress orientations measured by the hollow inclusion stress release method. This finding demonstrates that fault slip is controlled by NWW–NW faults that formed in a direction approximately parallel to the maximum principal stress oriented NNE–NE. These findings support the results of a previous study that attributed the stress orientation to fault slip control (Morris et al. 2016). The reconstruction results of the stress state in cluster 2, located in the middle of the field, display an

apparent departure from the regional stress tensor measured in this area. This finding suggests that cluster 2 does not correlate to the current regional stress field and thus may not be controlled by structural elements that trend NWW–NW. The preferred interpretation of the notable difference in the cumulative occurrence of events between cluster 1 and cluster 2, is that the deformation behaviors of ore deposits are influenced by the stress direction (Han 2016).

## 6 Conclusions

A geological environment and structural setting investigation is conducted in the Pingdingshan Deep No. 8 mine to analyze the relation between geologic structures and fault slip events. The field is a compressional basin intensively deformed by folds and faults with respect to a regional NE–SW stress field. Remarkable differences in the spatial trends of buried faults occur between different areas. The number of faults in the west and middle of the field is greater than that in the east of the field.

Analysis of events within the No. 8 mine reveal differences between the tectonic pattern and occurrence of fault slip. The relationships of fault slip with regional structural elements are studied in two main areas and suggests that cluster 1 is most likely controlled by the Guozhuang anticline; however, the reverse trapezoidal horst may create a greater energy release with fault slip. Cluster 2 is closely connected to the structurally controlled regular trapezoidal horst zones, and the force of friction is estimated to be rather low here.

Little evidence has been found to support the occurrence of fault slip dominated by event terrain curvature, the radius of curvature has an impressive correlation with the cumulative occurrence of fault slip in this area. More attention should be paid to the curvature range from  $1.0 \times 10^4$  to  $3.0 \times 10^4$ , and the radius of curvature likely acts as a prerequisite for dynamic sliding.

The distribution of events occurs in two areas corresponding to the apparent increased dip of the ore deposit zones. Furthermore, almost all of events concentrate at the edge of strata with extremely steep orebody dip gradients rather than within the interior of the inclined rock mass zones. This finding indicates



that layer-parallel faults could trigger these events due to a decrease in shear strength.

A stress inversion of the events in the west of the field shows that the local stress orientations are consistent with the focal mechanism inversion and measured results of the regional stress field. On the contrary, the results of events in the middle of the field manifests anomalous values and large rotation of the stress direction. Thus, it can be concluded that the maximum principal stress oriented NNE–NE exerts the primary control on the events in cluster 1, and the maximum principal stress oriented NWW–NW strongly influences the events in cluster 2. It has to be noted that the abovementioned conclusion is only for the case of events that occurred between 424 and 840 m depth. In this study, the structural elements and stress analyses have not explained mining-induced fault slip clearly; therefore, this conclusion is specific to the events that occurred in the No. 8 mine. The analysis conducted here is of value to other underground developments in structural zones and may show a positive effect on the general understanding of the prediction of the occurrence of fault slip.

**Acknowledgements** This study has been supported by the State Key Program of the National Natural Science Foundation of China, No. 41430640, and acknowledges the financial assistance of the National Natural Science Foundation of China, No. 41172144. Thanks also to Fuping Zhong for the helpful reviews of this manuscript.

## References

- Angelier J (1979) Determination of the mean principal direction of stresses for a given fault population. *Tectonophysics* 56:17–26
- Angelier J (1984) Tectonic analysis of fault slip data sets. *J Geophys Res* 89:5835–5848
- Angelier J, Tarantola A, Valette B, Manoussis S (1982) Inversion of field data in fault tectonics to obtain the regional stress—I. Single phase fault populations: a new method of computing the stress tensor. *Geophys J Int* 69:607–621
- Barton N (1982) Modelling rock joint behavior from in situ block tests: implications for nuclear waste repository design. Columbus: OH: office of nuclear waste isolation, pp. 96–97
- Bewick RP, Valley B, Runnals S, Whitney J, Krynicki Y (2009) Global approach to managing deep mining hazard. In: *Proceedings of the 3rd Can-US rock mechanics symposium*, Toronto
- Bonini M (2012) Mud volcanoes: indicators of stress orientation and tectonic controls. *Earth Sci Rev* 115:121–152
- Cai M, Kaiser PK, Tasaka Y, Maejima T, Morioka H, Minami M (2004) Generalized crack initiation and crack damage stress thresholds of brittle rock masses near underground excavations. *Int J Rock Mech Min Sci*. 41:833–847
- Coulson AL (1996) Mine induced seismicity in highly stressed ground: a case study—Creighton Mine Inco Ltd. Sudbury. Ph.D. thesis. Queen’s University, Canada
- Etchecopar A, Vasseur G, Daignieres M (1981) An inverse problem in microtectonics for the determination of stress tensors from fault striation analysis. *J Struct Geol*. 3:51–55
- Fehler M (1990) Identifying the plane of slip for a fault plane solution from clustering of locations of nearby earthquakes. *Geophys Res Lett* 17:969–972
- Feit GN, Malinnikova ON, Zykov VS (2002) Prediction of rockburst and sudden outburst hazard on the basis of estimate of rock-mass energy. *Int J Rock Mech Min Sci*. 38:61–63
- Frodsham K, Gayer RA (1999) The impact of tectonic deformation upon coal seams in the South Wales coalfield, UK. *Int J Coal Geol* 38:297–332
- Geological Survey of Henan Province (1990) Depositional models of coal-bearing sequences in the Henan province. China Geological University Press
- Guo T, Zeng P (2015) The structural and preservation conditions for shale gas enrichment and high productivity in the Wufeng-Longmaxi Formation, Southeastern Sichuan Basin. *Energy Explor Exploit* 33:259–276
- Han Y (2016) Deformation mechanisms and macromolecular structure response of anthracite under different stress. *Energy Fuels* 30:975–983
- Hatherly P (2013) Overview on the application of geophysics in coal mining. *Int J Coal Geol* 114:74–84
- Kalaneh S, Agh-Atabai M (2016) Spatial variation of earthquake hazard parameters in the Zagros fold and thrust belt SW Iran. *Nat Hazards* 82:933–946
- Kim Y-S, Peacock DCP, Sanderson DJ (2004) Fault damage zones. *J Struct Geol*. 26:503–517
- Li H (2001) Major and minor structural features of a bedding shear zone along a coal seam and related gas outburst, Pingdingshan coalfield, northern China. *Int J Coal Geol* 47:101–113
- Ma J, Ma S, Liu L (2002) Experimental study on patterns of fault interaction. *Progress Nat Sci* 12:503–508
- Marfurt KJ (2006) Robust estimates of 3D reflector dip and azimuth. *Geophysics* 71:29–40
- McGarr A, Bickness J, Sembera E, Green RWE (1989) Analysis of exceptionally large tremors in two gold mining districts of South Africa. *Pure Appl Geophys* 129:295–307
- Michael A, Ralf F, Bischoff M, Meier T (2009) Rock mechanical investigations of seismic events in a deep longwall coal mine. *Int J Rock Mech Min Sci* 46:408–420
- Morris AP, Ferrill DA, McGinnis RN (2016) Using fault displacement and slip tendency to estimate stress states. *J Struct Geol* 83:60–72
- Oettlea NK, Bray JD, Dreger DS (2015) Dynamic effects of surface fault rupture interaction with structures. *Soil Dyn Earthq Eng* 72:37–47
- Prudencio M, Jan MVS (2007) Strength and failure modes of rock mass models with non-persistent joints. *Int J Rock Mech Min Sci* 44:890–902

- Qu ZH (2010) Experimental study on the porous structure and compressibility of tectonized coals. *Energy Fuels* 24:2964–2973
- Roberts A (2001) Curvature attributes and their application to 3D interpreted horizons. *First Break* 19:85–100
- Sainoki Atsushi, Mitri Hani S (2014) Dynamic behaviour of mining-induced fault slip. *Int J Rock Mech Min Sci* 66:19–29
- Shi W, Cen M, Chen L, Wang Y, Chen X, Li J, Chen P (2015) Evolution of the late Cenozoic tectonic stress regime in the Shanxi Rift, central North China Plate inferred from new fault kinematic analysis. *J Asian Earth Sci* 114:54–72
- Sun M (2014) Study on in situ stress distribution law and its application in Pingdingshan mining Area. Ph.D. thesis. China University of Mining and Technology, Xuzhou
- Terakawa T, Yamanaka Y, Nakamichi H, Watanabe T, Yamazaki F, Horikawa S, Okuda T (2013) Effects of pore fluid pressure and tectonic stress on diverse seismic activities around the Mt. Ontake volcano, central Japan. *Tectonophysics* 608:138–148
- Wang F, Xu JL, Xie JL (2016) Mechanisms influencing the lateral roof roadway deformation by mining-induced fault population activation: a case study. *Int Oil Gas Coal Technol* 11:411–428
- Xiaojing Zhu, Yishan Pan, Zhi Tang (2015) Horst fault rockburst analysis based on shear beam theory. *Mech Eng* 37:182–189
- Xie Z, Liu Y, Hu W (2002) The focal mechanism of earthquake in Henan and its adjacent region. *Northwest Seismol J* 24:283–286
- Yadav DK, Hazarika D, Kumar N (2016) Seismicity and stress inversion study in the Kangra-Chamba region of north-west Himalaya. *Nat Hazards* 82:1393–1409
- Zeng L, Liu H (2009) The key geological factors influencing on development of low-permeability sandstone reservoirs: a case study of the Taizhao Area in the Songliao Basin, China. *Energy Explor Exploit* 27:425–437
- Zhang ZM (2009) Gas geology. Xuzhou: China University of Mining and Technology Press
- Zoback MD, Tsukahara H, Hickman S (1980) Stress measurements at depth in the vicinity of the San Andreas fault: implications for the magnitude of shear stress at depth. *J Geophys Res Solid Earth* 85:6157–6173